

# Coexistence of Type-II and Type-IV Dirac Fermions in SrAgBi

Tian-Chi Ma, Jing-Nan Hu, Yuan Chen, Lei Shao, Xian-Ru Hu, and Jian-Bo Deng\*

*Department of Physics, Lanzhou University,  
Lanzhou 730000, Peoples Republic of China*

(Dated: August 24, 2022)

## Abstract

Until now scientists have found three types of Dirac Fermions in crystals and these three types of Dirac Fermions can be described by one model. Here, we find a type of Dirac fermions that escapes this model. We find this type of Dirac fermions can exist in SrAgBi and is dubbed type-IV Dirac Fermions. The band near the type-IV Dirac points is nonlinear and the electron pocket and the hole pocket are from the same band. It is worth pointing out that there is a type-II Dirac Fermion near this new Dirac Fermion. So we used two models to describe the coexistence of these two Dirac fermions. Topological surface states of these two Dirac points are also calculated. We envision that our findings will stimulate researchers to study novel physics of type-IV Dirac fermions, as well as the interplay of type-II and type-IV Dirac fermions.

---

\* Jian-Bo Deng: dengjb@lzu.edu.cn

## I. INTRODUCTION

Dirac semimetals(DSMs) are currently drawing intense interest in condensed matter and materials physics [1–15]. They possess linearly-dispersing four-fold-degenerate Dirac points(DPs) close to the Fermi level. Dirac point can be regarded as two Weyl points [16–22] with opposite chirality meeting at the same  $k$ -point. The DSMs provide a fertile ground for exploring relativistic particles and high-energy phenomenology at the far more accessible solid-state physics scale. At present, Scientists have discovered three kinds of DSMs. The low-energy physics these three types of DSMs can be described by one model [7]:

$$H(\mathbf{k}) = \begin{bmatrix} h(\mathbf{k}) & \mathbf{0} \\ \mathbf{0} & h^*(-\mathbf{k}) \end{bmatrix} \quad (1)$$

with

$$h(\mathbf{k}) = \mathbf{v} \cdot \mathbf{k}\sigma_0 + \sum_{i,j} k_i A_{ij} \sigma_j, \quad (2)$$

where  $\sigma_0$  is the identity matrix and  $\sigma_j$  are Pauli matrices. The energy spectrum of a DP is

$$\begin{aligned} E_{\pm}(\mathbf{k}) &= \sum_i v_i k_i \pm \sqrt{\sum_j (\sum_i k_i A_{ij})^2} \\ &= T(\mathbf{k}) \pm U(\mathbf{k}). \end{aligned} \quad (3)$$

It is known that the band crossing point is a type-II DP if there exist a direction for which  $T > U$  [6, 23–25], otherwise it is a type-I DP [1, 3, 26–29]. If and only if for a particular direction  $\hat{k}$  in reciprocal space,  $T(\hat{k}) = U(\hat{k})$ , but  $T(\hat{k}) < U(\hat{k})$  for other directions, the DPs are connected by a line-like Fermi surface which is the Dirac line of the type-III DSM [7, 30–32]. The bands at the energy of DPs and the corresponding Fermi surfaces are shown in Fig. 1. One can find that the bands of these three types of Dirac semimetals near the DPs are all cones and the Fermi surface are Linear(For type-I DSM, Fermi surface degenerates to a point).

Recently, scientists discovered type-III Weyl points in  $(\text{TaSe}_4)_2\text{I}$  [33]. In  $(\text{TaSe}_4)_2\text{I}$ , the Fermi surface near the Weyl point consists of two electron or two hole pockets and these two pockets are from the same band and the band looks like a saddle. This discovery inspires us whether a similar situation exists in DSMs.

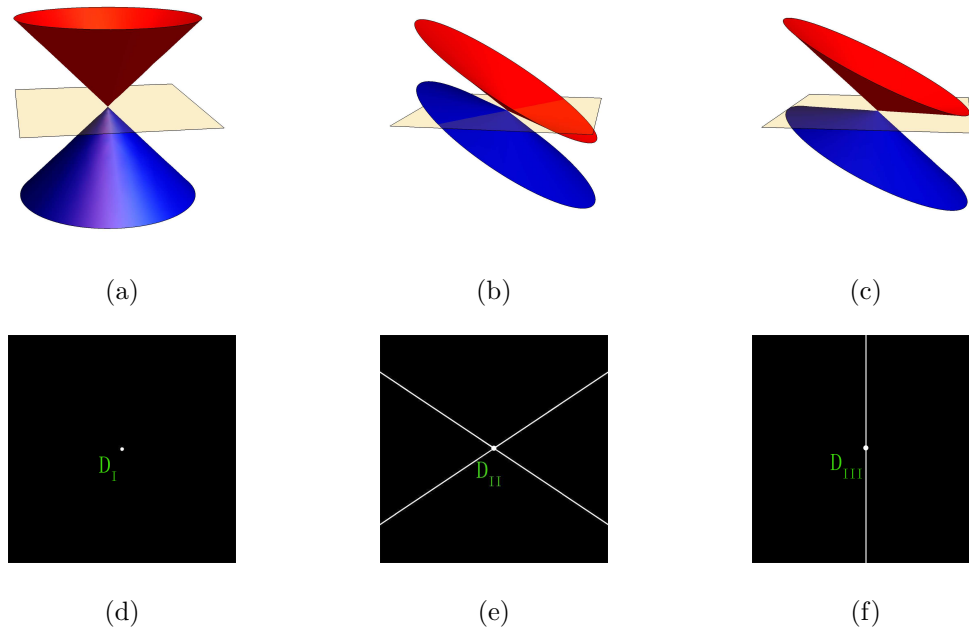


Figure 1: (a) Type-I DP with a point-like Fermi surface. (b) Type-II DP is the contact point between electron and hole pocket. (c) Type-III DP appears as the touching point between Dirac lines. The light yellow semitransparent plane corresponds to the position of the Fermi level. (d)-(f) Fermi surfaces of three types of DSMs.

In this work, we investigate type-II and type-IV Dirac fermions coexist in SrAgBi. Scientists' research interest in SrAgBi family materials has never been reduced [10, 34–41]. SrAgBi family materials were first predicted to exist DPs in Ref. (10). Later, CaAgBi was predicted to coexist type-I and type-II Dirac fermions in Ref. (34).

Here, we studied a new type of Dirac fermions in SrAgBi and is dubbed type-IV Dirac Fermions. At the energy of type-IV Dirac fermions, the Fermi surface consists of a electron pocket and a hole pocket, it is similar to type-II Dirac Fermions, but the bands are non-linear. The electron pocket is in the hole pocket and they touch at the DPs. The Fermi arcs of both DPs were clearly discovered. Meanwhile, we use a eight-band  $k\cdot p$  model to discribe the bandcrossing near the Fermi level along  $\Gamma$ -A. More importantly, we reproduce the bands of SrAgBi near the Fermi level with a tight-binding model. The Fermi surface of this model is consistent with the result of first-principles band-structure calculations.

## II. COMPUTATION METHODS

In this paper, density-functional theory (DFT) calculations with the projected augmented wave (PAW) are implemented in the VASP [42, 43] with generalized gradient approximation (GGA) [44]. The spin-orbit coupling (SOC) was employed in the electronic structure calculations. The tight-binding model matrix elements are calculated by projecting onto the Wannier orbitals [45–47]. We used Sr  $d$ -orbitals, Ag  $d$ -orbitals and Bi  $p$ -orbitals as initial wave functions for maximizing localization. Surface spectra were calculated based on the iterative Greens function with the help of WannierTools [48]. The eight-band tight-binding model is calculated by PythTB [49].

### III. RESULTS

#### A. Electronic structure

The SrAgBi family of compounds crystalizes in a hexagonal Bravais lattice with space group  $D_{6h}^4$  ( $P6_3/mmc$ , No. 194). As shown in Fig. 2(a) and 2(b). The crystal structure can be viewed as stacked graphene layers; the  $\text{Sr}^{2+}$  cations are stacked between  $[\text{Ag}^{1+}\text{As}^{3-}]^{2-}$  in the honeycomb network. Fig. 3(a) shows the bulk and surface Brillouin zone (BZ) of SrAgBi crystal. The type-II and type-IV DPs are marked by green points and blue points, respectively.

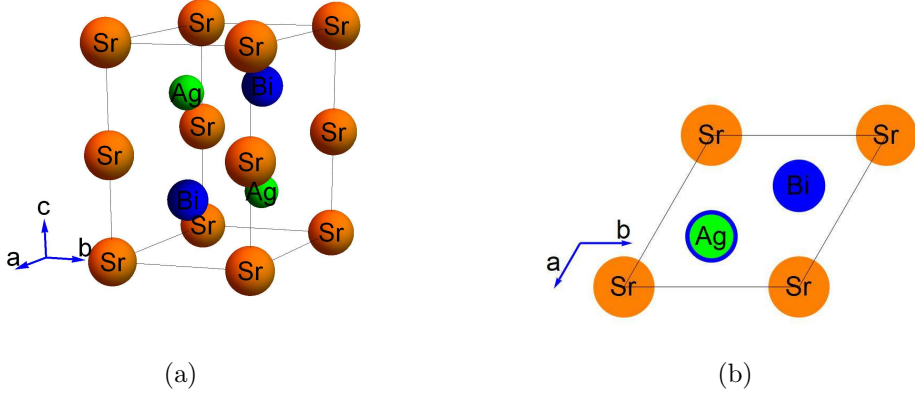


Figure 2: (a) Side view and (b) top view of the crystal structure of SrAgBi.

We now present the calculated band structure of SrAgBi to reveal the DPs and its type-IV character. The calculated bulk band structure along high symmetry directions [Fig. 3(b)] reveals the semimetallic ground state. The band structure shows that there are two DPs along the  $\Gamma$ -A direction. We mark these two DPs in Fig. 3(c). The blue one is type-IV DP and the green one is type-II DP. Figure 3(d) shows the three dimensions (3D) band structure of valance band and conduction band and they touch at type-IV DPs. One can find that the band structure near a

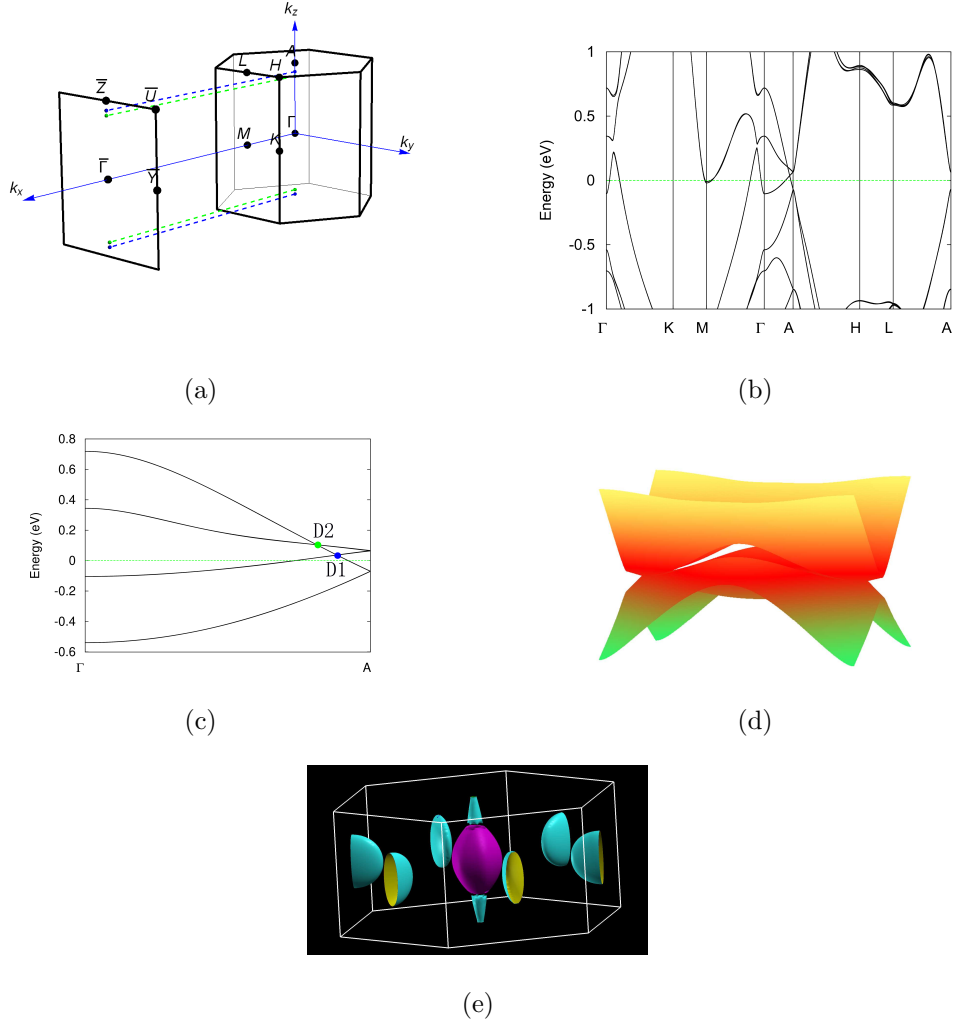


Figure 3: (a) BZ of bulk and the projected surface BZ of (100) plane. Band structure on high symmetry line (b), (c) and  $k_y - k_z$  plane (d). (e) Bulk-state equal-energy contours of  $E = 0.1043$  eV.

type-IV DP isn't a perfect cone and can't be described by equation (1). Because a type-IV Dirac node exists between  $\Gamma$  and  $A$  points, and the two planes  $k_z = 0$ ,  $k_z = \pi$  are fully gapped, the two dimensions (2D) topological invariants of the two planes

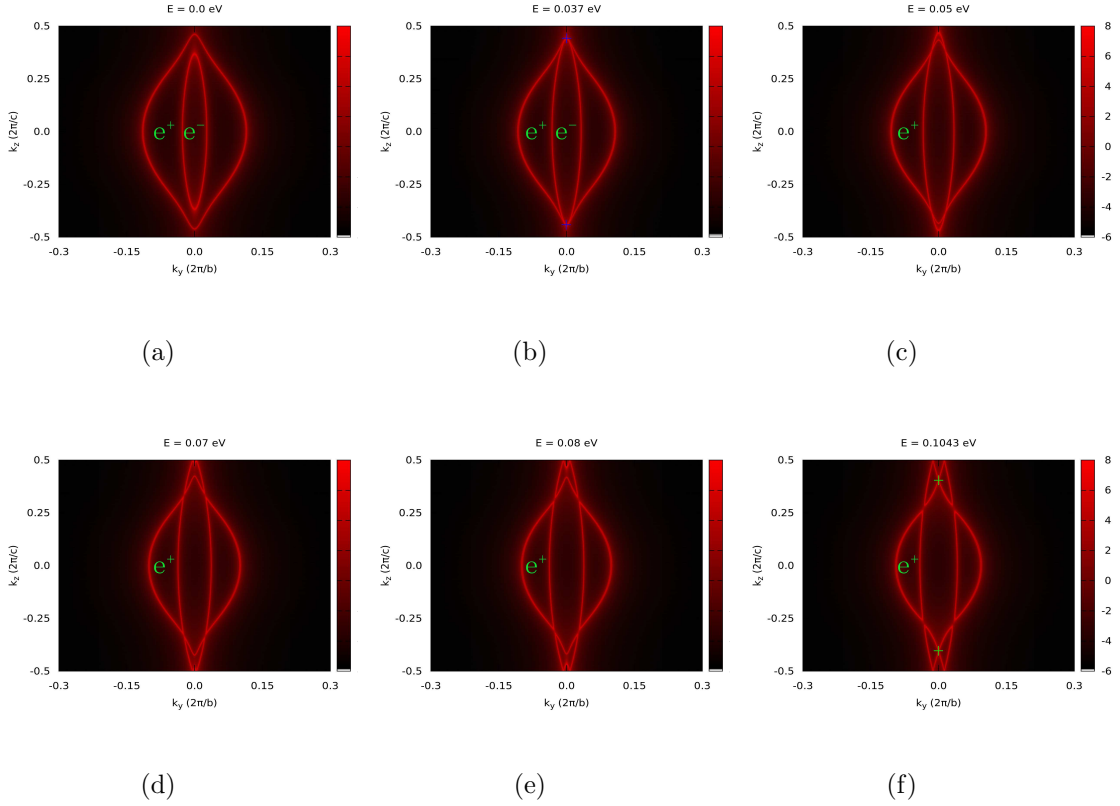


Figure 4: Bulk constant energy contours in  $(k_y, k_z)$  space at  $k_x = 0$  of different energy around the Fermi level.

must be topologically distinct. For the illustration, one can consider their 2D  $Z_2$  invariants [50],  $\nu_0$  and  $\nu_\pi$ . Using the Fu-Kane method [51], one results that  $(\nu_0, \nu_\pi) = (1, 0)$ . These two invariants indicate the single band inversion at  $\Gamma$ .

Because the type-II DP and the type-IV DP are formed by the intersection of three adjacent bands and they are very close to each other in BZ, We think it is meaningful to study the relationship between these two points. Fig. 4 shows the evolution of bulk-state equal-energy contours for different values of E, the blue “+”

is the position of type-IV DP and the green “+” is the position of type-II DP.  $e^+$  and  $e^-$  represent hole pocket and electron pocket, respectively. When  $E = 0.0$  eV, there is a electron pocket in a hole pocket. When  $E = 0.037$  eV, the energy of type-IV DP, the electron pocket touches the hole pocket. The touched points are type-IV DPs. When the energy continues to increase, the electron pocket disappears and when  $E = 0.1043$  eV, the other two pockets touch at type-II DPs.

### B. Fermi arcs and surface states

Fermi arc electron states on the surface of the crystal are the signature of the Dirac semimetal state. In our case, we present calculations of the (100) surface states. Figures 5(a) and 5(b) are (100) Fermi surfaces for type-IV and type-II DPs. There exist the Fermi arcs marked by the arrows and the Fermi arcs are terminating at the projected DPs. Figure 5(c) shows the enlarged view of the area highlighted by the black box in Fig. 5(b). Figure 5(d) shows the energy dispersion of the surface band structure along  $\bar{\Gamma}-\bar{A}$  ( $k_z$ ) direction. The projected Dirac points are denoted as a blue “+” and a green “+” respectively. We observe surface states that emerge out of the DPs at  $k_z=0.406(2\pi/c)$  and  $k_z=0.438(2\pi/c)$ .

## IV. MODELS

Now we begin to illustrate the type-IV DSM phase in a simplified model. Consider two pairs of DPs located on  $\Gamma$ -A in the BZ. Here,  $\Gamma$ -A is the principal rotation axis, which offers the symmetry protection needed for the DPs [52]. Because the nontrivial band inversion of SrAgBi is determined by the low-energy bands along  $\Gamma$ -A, while the bands elsewhere are far away from Fermi level. To describe SrAgBi, we need an eight-band model, because of the following considerations. (i) There are two pairs of

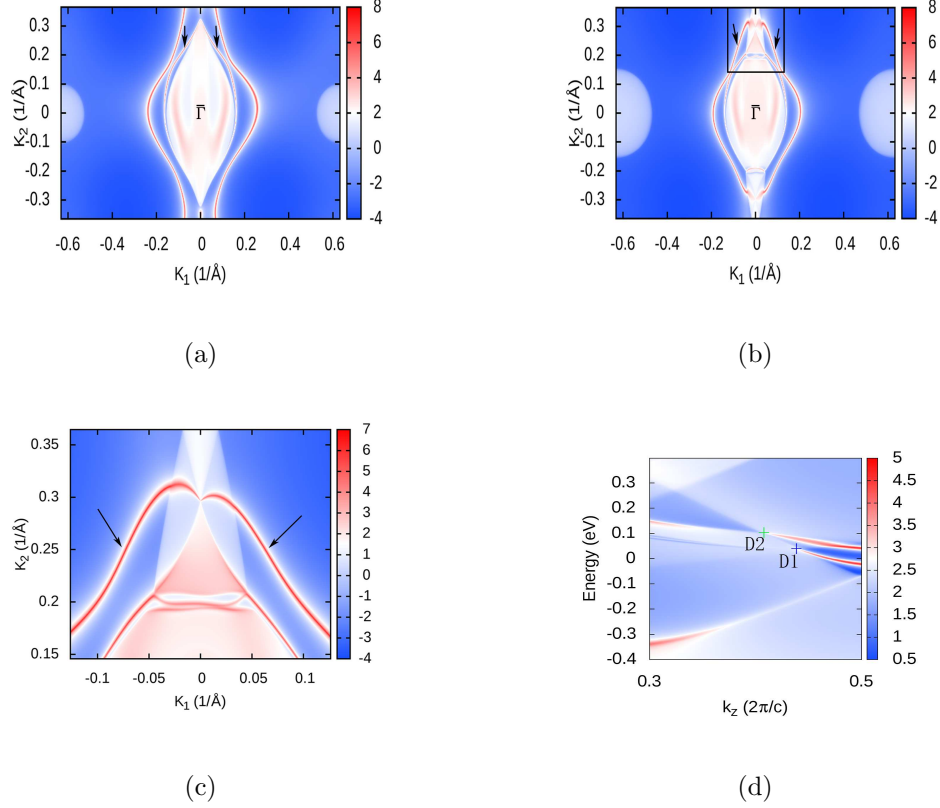


Figure 5: Surface Fermi surface with SOC of (a) at the energy of type-IV DPs and (b) at the energy of type-II DPs. (c) An enlarged view of the area highlighted by the black box in (b). (d) Surface band structure of SrAgBi along the  $\bar{\Gamma}$ - $\bar{A}$  direction on the (100) surface BZ.

bands near the Fermi level. (ii) One band crosses the other two bands with different symmetry characters to form the DPs. (iii) Each band should be Kramers degenerate in the presence of both time-reversal( $\mathcal{T}$ ) and inversion( $\mathcal{P}$ ).

With the reasons above, we consider the following model defined around  $\Gamma$ -A [15]:

$$\mathcal{H}_{\text{eff}} = \begin{bmatrix} H_{\uparrow\uparrow} & \mathbf{0} \\ \mathbf{0} & H_{\downarrow\downarrow} \end{bmatrix}, \quad (4)$$

where  $H_{\uparrow\uparrow}$  and  $H_{\downarrow\downarrow}$  are  $4 \times 4$  matrices with

$$H_{\uparrow\uparrow} = \begin{bmatrix} M_1 & B_1 \cos \frac{k_z}{2} & 0 & Ak_+ \\ B_1 \cos \frac{k_z}{2} & M_1 & Ak_+ & 0 \\ 0 & Ak_- & M_2 & B_2 \cos \frac{k_z}{2} \\ Ak_- & 0 & B_2 \cos \frac{k_z}{2} & M_2 \end{bmatrix} \quad (5)$$

and  $H_{\downarrow\downarrow} = H_{\uparrow\uparrow}^*$ . Here,  $k_{\pm} = k_x \pm ik_y$  and  $A$ ,  $B_i$ , and  $M_i$  ( $i = 1, 2$ ) are the parameters of the model. On the  $\Gamma$ -A path in which  $k_{\pm} = 0$ , one obtains the following Kramers degenerate spectrum:

$$\varepsilon_{i,\pm}(k_z) = M_i \pm B_i \cos \frac{k_z}{2}. \quad (6)$$

At  $\Gamma$  and A, the band energies respectively are

$$\varepsilon_{i,\pm}^{\Gamma} = M_i \pm B_i, \quad \varepsilon_{i,\pm}^A = M_i. \quad (7)$$

By tuning  $M_i$  and  $B_i$ , the band structures for equation (4) can drop into three distinct cases, as shown in Fig. 6. We assume that in the atomic limit the pair  $\varepsilon_{1,\pm}$  is energetically above  $\varepsilon_{2,\pm}$ , and consider the bands are half-filled. The case in Fig. 6(a) is a trivial insulating phase adiabatically connected to the atomic limit. For the case in Fig. 6(b), there is only one band inversion at  $\Gamma$ , leading to the formation of DPs. For the case in Fig. 6(c), there are two band inversions at  $\Gamma$ , this situation is consistent with SrAgBi.

The above analysis provides an intuitive picture of the band inversion and band crossing along  $\Gamma$ -A of the type-IV DSM phase, yet the symmetry protections cannot be captured within the simplified model. To fully characterize the type-IV DSM

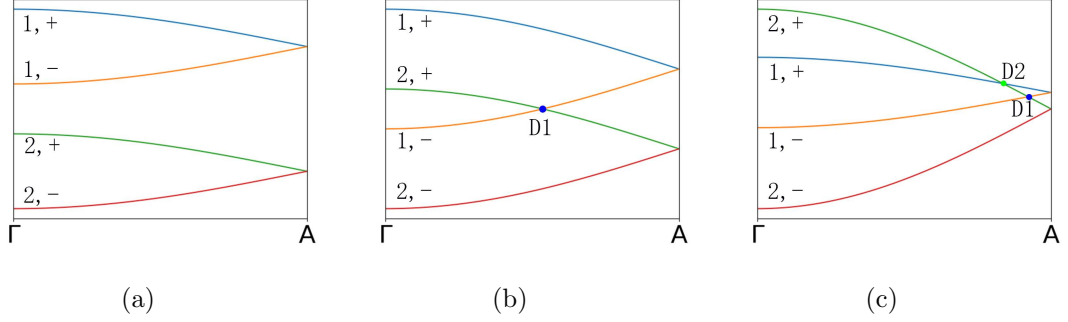


Figure 6: Three types of phases with distinct band ordering along the  $\Gamma$ - $A$  path, as described by the Eq. (4). (c) is consistent with the band of SrAgBi along  $\Gamma$ - $A$  near the Fermi energy.

phase, we extend the simplified equation (4) to a tight-binding model. SrAgBi has three important symmetries in addition to the  $\mathcal{T}$  and  $\mathcal{P}$ : A sixfold screw rotation  $\tilde{C}_6 : (x, y, z) \rightarrow (x/2 - \sqrt{3}y/2, \sqrt{3}x/2 + y/2, z + 1/2)$ , a horizontal mirror  $M_z : (x, y, z) \rightarrow (x, y, -z + 1/2)$ , and a vertical glide mirror  $\tilde{M}_y : (x, y, z) \rightarrow (x, -y, z + 1/2)$ . According to the first principle calculation, we find that almost all of the electron state near the fermi energy come from  $Ag$ 's  $d$  orbital and  $Bi$ 's  $p$  orbital. So we consider a 3D lattice consisting of 2D honeycomb layers stacked along  $z$ , as sketched in Fig. 7(a). For each layer, the  $A$  and  $B$  sites are occupied by two different types of atoms,  $Ag$  and  $Bi$ , respectively. Each unit cell contains two layers, between which  $A$  and  $B$  are switched. We assume that each site has two basis orbitals forming a Kramers pair:  $|p_+, \uparrow\rangle$  and  $|p_-, \downarrow\rangle$  on  $A$ , whereas  $|d_{+2}, \uparrow\rangle$  and  $|d_{-2}, \downarrow\rangle$  on  $B$ . where  $p_{\pm} = p_x \pm ip_y$  and  $d_{\pm 2} = d_{x^2-y^2} \pm 2id_{xy}$ . Based on these, we use the following

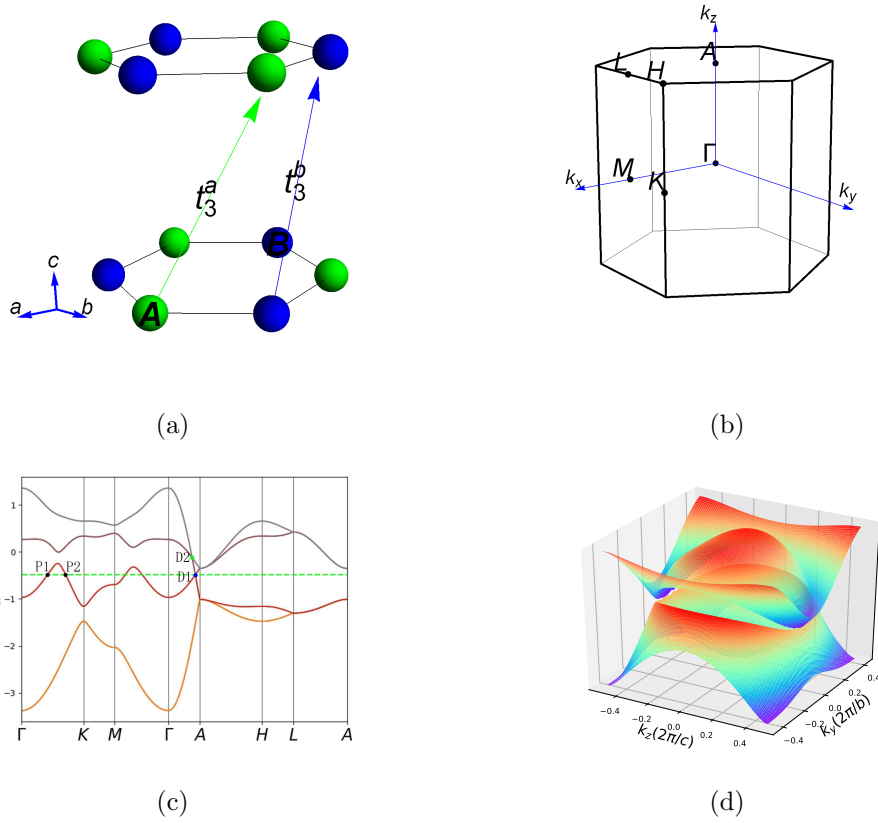


Figure 7: (a) 3D lattice model. The arrows indicate two interlayer hopping processes. (b) The bulk BZ of this model. (c) Band structure of the model. (d) 3D band structure on  $k_y - k_z$  plane; we have used  $\epsilon_a = -1.1083$  eV,  $\epsilon_b = 0.1087$  eV,  $t_1 = 0.2533$  eV,  $t_2^a = 0.0166$  eV,  $t_2^b = -0.0766$  eV,  $t_3^a = -0.3950$  eV,  $t_3^b = -0.1030$  eV.

tight-binding model [15]:

$$\begin{aligned}
\mathcal{H} = & \sum_{\alpha,i} (\epsilon_a a_{\alpha,i}^\dagger a_{\alpha,i} + \epsilon_b b_{\alpha,i}^\dagger b_{\alpha,i}) \\
& + \sum_{\alpha,i,m} t_1 (-1)^\alpha (a_{\alpha,i+\mathbf{R}_m}^\dagger \sigma_z e^{i(2m-1)\pi/3} b_{\alpha,i} + \text{H.c.}) \\
& + \sum_{\alpha,i,n} (t_2^a a_{\alpha,i+\mathbf{R}'_n}^\dagger a_{\alpha,i} + t_2^b b_{\alpha,i+\mathbf{R}'_n}^\dagger b_{\alpha,i}) \\
& + \sum_{i,m} (t_3^a a_{0,i+\mathbf{R}_m}^\dagger a_{1,i} + t_3^b b_{1,i+\mathbf{R}_m}^\dagger b_{0,i} + \text{H.c.}).
\end{aligned} \tag{8}$$

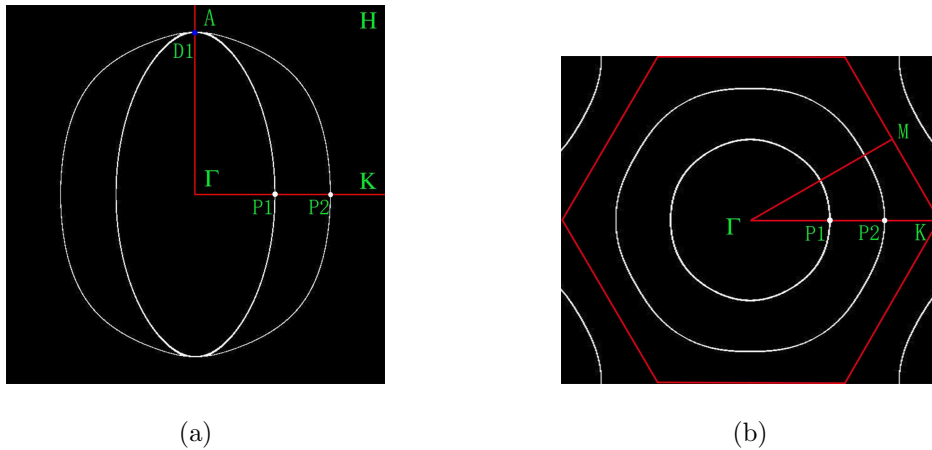


Figure 8: (a)  $k_y - k_z$  and (b)  $k_x - k_y$  plane bulk-state equal-energy contours.

Here,  $a^\dagger = (a_{|p_+, \uparrow}^\dagger, a_{|p_-, \downarrow}^\dagger)$  and  $b^\dagger = (b_{|d_+, \uparrow}^\dagger, b_{|d_-, \downarrow}^\dagger)$  are the electron creation operators,  $\alpha = 0, 1$  label the two layers in a unit cell,  $i$  labels the sites within a layer,  $\mathbf{R}_m$  ( $m = 1, 2, 3$ ) correspond to the vectors connecting to the three nearest neighbors in a layer,  $\mathbf{R}'_n$  ( $n = 1, \dots, 6$ ) correspond to the vectors connecting to the six next-nearest neighbors in a layer,  $\epsilon_a$  and  $\epsilon_b$  are the on-site energies, and the  $t$ 's are various hopping amplitudes (taken to be real). In model (8), the first term represents an on-site energy difference, and the second and third terms are hoppings within a honeycomb layer, with the extra phase factor due to the different orbital characters

on  $A$  and  $B$ . In this model, the nearest interlayer hopping is suppressed as the two orbitals involved have different angular momenta along  $z$ . Thus, the strongest interlayer hopping, i.e., the last term in model (8), occurs between two  $A$  or two  $B$  sites, as indicated in Fig. 7(a). This model retains the main symmetry of SrAgBi. If the Sr atoms in SrAgBi were removed, the crystal lattice would become identical to the lattice for this tight-binding model.

Figures 7(c) and 7(d) show the band structure of the type-IV DSM phase in the tight-binding model (8), and the low-energy physics resembles that in Fig. 3(b) and 3(d). One can see that there is part of valance band (P1-P2) along  $\Gamma$ -K in Fig. 7(c), which is higher than the Fermi level, this is very important in forming type-IV DPs. Figures 8(a) and 8(b) show the bulk-state equal-energy contours of  $k_y - k_z$  and  $k_z = 0$  plane, this means that there is a electron pocket in a hole pocket and these two pockets touch at type-IV DPs. One can find Fig. 8(a) is similar to Fig. 4(b), this proves that the model we chose is effective in describing SrAgBi.

## V. CONCLUSION

By using the first principle calculation with SOC, we proposed that type-IV Dirac fermions exist in the bulk state of SrAgBi. Distinct from type-I, type-II and type-III Dirac semimetals such as Na<sub>3</sub>Bi [1], VGa<sub>3</sub> [6] and Zn<sub>2</sub>In<sub>2</sub>S<sub>5</sub> [7], SrAgBi has nonlinear bands near the type-IV DPs. Because there is a type-II DP near the type-IV DP, SrAgBi provides a platform for exploring the interplay between type-II and type-IV Dirac fermions, we used two models to describe the coexistence of these two Dirac fermions. Topological surface states of these two DPs are also calculated. The bulk DPs and the surface states can be experimentally probed by the angle-resolved photoemission spectroscopy (ARPES) [2, 18]. In addition, some articles point out that by doping other atoms, one DP in this type of material can be split into two

triple points [38, 53], which points out the direction for our future work.

---

- [1] Zhijun Wang, Yan Sun, Xing-Qiu Chen, Cesare Franchini, Gang Xu, Hongming Weng, Xi Dai, and Zhong Fang. Dirac semimetal and topological phase transitions in  $A_3\text{Bi}$  ( $A = \text{Na}, \text{K}, \text{Rb}$ ). *Physical Review B*, 85(19):195320, 2012.
- [2] ZK Liu, Bo Zhou, Yong Zhang, ZJ Wang, HM Weng, Dharmalingam Prabhakaran, S-K Mo, ZX Shen, Zhong Fang, Xi Dai, et al. Discovery of a Three-Dimensional Topological Dirac Semimetal,  $\text{Na}_3\text{Bi}$ . *Science*, 343(6173):864–867, 2014.
- [3] ZK Liu, Jianzhong Jiang, Bo Zhou, ZJ Wang, Yi Zhang, HM Weng, Dharmalingam Prabhakaran, Sung Kwan Mo, Han Peng, Pavel Dudin, et al. A stable three-dimensional topological Dirac semimetal  $\text{Cd}_3\text{As}_2$ . *Nature materials*, 13(7):677–681, 2014.
- [4] Tian Liang, Quinn Gibson, Mazhar N Ali, Minhao Liu, RJ Cava, and NP Ong. Ultrahigh mobility and giant magnetoresistance in the Dirac semimetal  $\text{Cd}_3\text{As}_2$ . *Nature materials*, 14(3):280–284, 2015.
- [5] Sergey Borisenko, Quinn Gibson, Danil Evtushinsky, Volodymyr Zabolotnyy, Bernd Büchner, and Robert J Cava. Experimental Realization of a Three-Dimensional Dirac Semimetal. *Physical review letters*, 113(2):027603, 2014.
- [6] Tay-Rong Chang, Su-Yang Xu, Daniel S Sanchez, Wei-Feng Tsai, Shin-Ming Huang, Guoqing Chang, Chuang-Han Hsu, Guang Bian, Ilya Belopolski, Zhi-Ming Yu, et al. Type-II symmetry-protected topological Dirac semimetals. *Physical review letters*, 119(2):026404, 2017.
- [7] Huaqing Huang, Kyung-Hwan Jin, and Feng Liu. Black Hole Horizon in a Type-III Dirac Semimetal  $\text{Zn}_2\text{In}_2\text{S}_5$ . *arXiv preprint arXiv:1711.07096*, 2017.

- [8] M Milićević, G Montambaux, T Ozawa, I Sagnes, A Lemaître, L Le Gratiet, A Harouri, J Bloch, and A Amo. Tilted and type-III Dirac cones emerging from flat bands in photonic orbital graphene. *arXiv preprint arXiv:1807.08650*, 2018.
- [9] Steve M Young, Saad Zaheer, Jeffrey CY Teo, Charles L Kane, Eugene J Mele, and Andrew M Rappe. Dirac semimetal in three dimensions. *Physical review letters*, 108(14):140405, 2012.
- [10] QD Gibson, Leslie Mareike Schoop, L Muechler, LS Xie, M Hirschberger, Nai Phuan Ong, Roberto Car, and Robert Joseph Cava. Three-dimensional Dirac semimetals: Design principles and predictions of new materials. *Physical Review B*, 91(20):205128, 2015.
- [11] Steve M Young and Charles L Kane. Dirac semimetals in two dimensions. *Physical review letters*, 115(12):126803, 2015.
- [12] RY Chen, SJ Zhang, JA Schneeloch, C Zhang, Q Li, GD Gu, and NL Wang. Optical spectroscopy study of the three-dimensional Dirac semimetal ZrTe<sub>5</sub>. *Physical Review B*, 92(7):075107, 2015.
- [13] Benjamin J Wieder, Youngkuk Kim, AM Rappe, and CL Kane. Double Dirac semimetals in three dimensions. *Physical review letters*, 116(18):186402, 2016.
- [14] Mario Novak, Satoshi Sasaki, Kouji Segawa, and Yoichi Ando. Large linear magnetoresistance in the Dirac semimetal TlBiSSe. *Physical Review B*, 91(4):041203, 2015.
- [15] Ziming Zhu, Zhi-Ming Yu, Weikang Wu, Lifa Zhang, Wei Zhang, Fan Zhang, and Shengyuan A Yang. Composite Dirac semimetals. *Physical Review B*, 100(16):161401, 2019.
- [16] Xiangang Wan, Ari M Turner, Ashvin Vishwanath, and Sergey Y Savrasov. Topological semimetal and Fermi-arc surface states in the electronic structure of pyrochlore iridates. *Physical Review B*, 83(20):205101, 2011.

- [17] AA Burkov and Leon Balents. Weyl semimetal in a topological insulator multilayer. *Physical review letters*, 107(12):127205, 2011.
- [18] Su-Yang Xu, Ilya Belopolski, Nasser Alidoust, Madhab Neupane, Guang Bian, Chenglong Zhang, Raman Sankar, Guoqing Chang, Zhujun Yuan, Chi-Cheng Lee, et al. Discovery of a Weyl fermion semimetal and topological Fermi arcs. *Science*, 349(6248):613–617, 2015.
- [19] Hongming Weng, Chen Fang, Zhong Fang, B Andrei Bernevig, and Xi Dai. Weyl semimetal phase in noncentrosymmetric transition-metal monophosphides. *Physical Review X*, 5(1):011029, 2015.
- [20] Ling Lu, Zhiyu Wang, Dexin Ye, Lixin Ran, Liang Fu, John D Joannopoulos, and Marin Soljačić. Experimental observation of Weyl points. *Science*, 349(6248):622–624, 2015.
- [21] BQ Lv, HM Weng, BB Fu, X Ps Wang, Hu Miao, Junzhang Ma, P Richard, XC Huang, LX Zhao, GF Chen, et al. Experimental discovery of Weyl semimetal TaAs. *Physical Review X*, 5(3):031013, 2015.
- [22] Alexey A Soluyanov, Dominik Gresch, Zhijun Wang, QuanSheng Wu, Matthias Troyer, Xi Dai, and B Andrei Bernevig. Type-II weyl semimetals. *Nature*, 527(7579):495–498, 2015.
- [23] Mingzhe Yan, Huaqing Huang, Kenan Zhang, Eryin Wang, Wei Yao, Ke Deng, Guoliang Wan, Hongyun Zhang, Masashi Arita, Haitao Yang, et al. Lorentz-violating type-II Dirac fermions in transition metal dichalcogenide PtTe<sub>2</sub>. *Nature communications*, 8(1):1–6, 2017.
- [24] Huaqing Huang, Shuyun Zhou, and Wenhui Duan. Type-ii dirac fermions in the ptse<sub>2</sub> class of transition metal dichalcogenides. *Physical Review B*, 94(12):121117, 2016.
- [25] Kenan Zhang, Mingzhe Yan, Haoxiong Zhang, Huaqing Huang, Masashi Arita, Zhe Sun, Wenhui Duan, Yang Wu, and Shuyun Zhou. Experimental evidence for type-ii

- dirac semimetal in  $\text{PtSe}_2$ . *Physical Review B*, 96(12):125102, 2017.
- [26] RC Xiao, PL Gong, QS Wu, WJ Lu, MJ Wei, JY Li, HY Lv, X Luo, P Tong, XB Zhu, et al. Manipulation of type-I and type-II Dirac points in  $\text{PdTe}_2$  superconductor by external pressure. *Physical Review B*, 96(7):075101, 2017.
- [27] Hang Liu, Jia-Tao Sun, and Sheng Meng. Engineering dirac states in graphene: Co-existing type-i and type-ii floquet-dirac fermions. *Physical Review B*, 99(7):075121, 2019.
- [28] Weifeng Li, Meng Guo, Gang Zhang, and Yong-Wei Zhang. Gapless mos 2 allotrope possessing both massless dirac and heavy fermions. *Physical Review B*, 89(20):205402, 2014.
- [29] Søren Ulstrup, Jens Christian Johannsen, Federico Cilento, Jill A Miwa, Alberto Crepaldi, Michele Zacchigna, Cephise Cacho, Richard Chapman, Emma Springate, Samir Mammadov, et al. Ultrafast dynamics of massive Dirac fermions in bilayer graphene. *Physical review letters*, 112(25):257401, 2014.
- [30] M Milićević, G Montambaux, T Ozawa, O Jamadi, B Real, I Sagnes, A Lemaître, L Le Gratiet, A Harouri, J Bloch, et al. Type-III and tilted Dirac cones emerging from flat bands in photonic orbital graphene. *Physical Review X*, 9(3):031010, 2019.
- [31] L Jin, HC Wu, Bo-Bo Wei, and Z Song. Hybrid exceptional point created from type-III Dirac point. *Physical Review B*, 101(4):045130, 2020.
- [32] Zhenhao Gong, Xizhi Shi, Jin Li, Shifang Li, Chaoyu He, Tao Ouyang, Chunxiao Zhang, Chao Tang, and Jianxin Zhong. Theoretical prediction of low-energy stone-wales graphene with an intrinsic type-iii dirac cone. *Physical Review B*, 101(15):155427, 2020.
- [33] Xiao-Ping Li, Ke Deng, Botao Fu, YongKai Li, DaShuai Ma, JunFeng Han, Jianhui Zhou, Shuyun Zhou, and Yugui Yao. Type-III Weyl Semimetals and its Materialization. *arXiv preprint arXiv:1909.12178*, 2019.

- [34] Cong Chen, Shan-Shan Wang, Lei Liu, Zhi-Ming Yu, Xian-Lei Sheng, Ziyu Chen, and Shengyuan A Yang. Ternary wurtzite CaAgBi materials family: A playground for essential and accidental, type-I and type-II Dirac fermions. *Physical Review Materials*, 1(4):044201, 2017.
- [35] Cong Chen, Shan-Shan Wang, Lei Liu, Zhi-Ming Yu, Xian-Lei Sheng, Ziyu Chen, and Shengyuan A Yang. Hybrid Dirac Semimetal in CaAgBi Materials Family. *arXiv preprint arXiv:1706.03915*, 2017.
- [36] Souvik Sasmal, Rajib Mondal, Ruta Kulkarni, Arumugam Thamizhavel, and Bahadur Singh. Magnetotransport properties of noncentrosymmetric CaAgBi single crystal. *Journal of Physics: Condensed Matter*, 32(33):335701, 2020.
- [37] YS Chai, X Ding, V Zapf, and TL Xia. Confirmation of Dirac Semimetal in CaAgBi by magnetostriction measurements.
- [38] Sougata Mardanya, Bahadur Singh, Shin-Ming Huang, Tay-Rong Chang, Chenliang Su, Hsin Lin, Amit Agarwal, and Arun Bansil. Prediction of threefold fermions in a nearly ideal Dirac semimetal BaAgAs. *Physical Review Materials*, 3(7):071201, 2019.
- [39] Sheng Xu, Huan Wang, Yi-Yan Wang, Yuan Su, Xiao-Yan Wang, and Tian-Long Xia. Crystal growth of BaAgAs family topological materials via flux method. *Journal of Crystal Growth*, 531:125304, 2020.
- [40] Kosuke Nakayama, Zhiwei Wang, Daichi Takane, Seigo Souma, Yuya Kubota, Yuki Nakata, Cephise Cacho, Timur Kim, Sandy Adhitha Ekahana, Ming Shi, et al. Observation of inverted band structure in the topological Dirac semimetal candidate CaAuAs. *Physical Review B*, 102(4):041104, 2020.
- [41] Tommy Tai and Ching Hua Lee. Anisotropic non-linear optical response of nodal loop materials. *arXiv preprint arXiv:2006.16851*, 2020.
- [42] John P Perdew and Alex Zunger. Self-interaction correction to density-functional approximations for many-electron systems. *Physical Review B*, 23(10):5048, 1981.

- [43] Georg Kresse and Jürgen Furthmüller. Efficiency of ab-initio total energy calculations for metals and semiconductors using a plane-wave basis set. *Computational materials science*, 6(1):15–50, 1996.
- [44] John P Perdew, Kieron Burke, and Matthias Ernzerhof. Generalized gradient approximation made simple. *Physical review letters*, 77(18):3865, 1996.
- [45] Nicola Marzari and David Vanderbilt. Maximally localized generalized Wannier functions for composite energy bands. *Physical review B*, 56(20):12847, 1997.
- [46] Ivo Souza, Nicola Marzari, and David Vanderbilt. Maximally localized Wannier functions for entangled energy bands. *Physical Review B*, 65(3):035109, 2001.
- [47] Arash A Mostofi, Jonathan R Yates, Giovanni Pizzi, Young-Su Lee, Ivo Souza, David Vanderbilt, and Nicola Marzari. An updated version of wannier90: A tool for obtaining maximally-localised Wannier functions. *Computer Physics Communications*, 185(8):2309–2310, 2014.
- [48] QuanSheng Wu, ShengNan Zhang, Hai-Feng Song, Matthias Troyer, and Alexey A Soluyanov. WannierTools: An open-source software package for novel topological materials. *Computer Physics Communications*, 224:405–416, 2018.
- [49] Tahir Yusufaly, David Vanderbilt, and Sinisa Coh. Tight-Binding Formalism in the Context of the PythTB Package, 2013.
- [50] Charles L Kane and Eugene J Mele.  $Z_2$  topological order and the quantum spin Hall effect. *Physical review letters*, 95(14):146802, 2005.
- [51] Liang Fu and Charles L Kane. Topological insulators with inversion symmetry. *Physical Review B*, 76(4):045302, 2007.
- [52] Bohm-Jung Yang and Naoto Nagaosa. Classification of stable three-dimensional Dirac semimetals with nontrivial topology. *Nature communications*, 5(1):1–10, 2014.
- [53] Chiranjit Mondal, CK Barman, Aftab Alam, and Biswarup Pathak. Broken symmetry driven topological semi-metal to gaped phase transitions in SrAgAs. *arXiv preprint*

*arXiv:1811.06685*, 2018.